Utah State University

DigitalCommons@USU

Publications   Atmospheric Imaging Laboratory

8-20-2014

A coordinated investigation of the gravity wave breaking and the associated dynamical instability by a Na lidar and an Advanced Mesosphere Temperature Mapper over Logan, UT (41.7°N, 111.8°W)

Xuguang Cai
Utah State University

Tao Yuan
Utah State University, titus.yuan@usu.edu

Yucheng Zhao
Utah State University, yu.cheng@usu.edu

Pierre-Dominique Pautet
Utah State University, dominiquepautet@gmail.com

Michael J. Taylor
Utah State University, mike.taylor@usu.edu

William R. Pendleton Jr.
Utah State University

Recommended Citation

UtahState University
MERRILL-CAZIER LIBRARY

RESEARCH ARTICLE

Key Points:
- Na lidar and AMTM investigation of MLT
- Small-scale gravity wave breaking due to dynamic instability
- Large-amplitude gravity wave induces dynamic instability

Correspondence to:
T. Yuan,
titus.yuan@usu.edu

A coordinated investigation of the gravity wave breaking and the associated dynamical instability by a Na lidar and an Advanced Mesosphere Temperature Mapper over Logan, UT (41.7°N, 111.8°W)

Xuguang Cai[1,2], Tao Yuan[1], Yucheng Zhao[1], Pierre-Dominique Pautet[1], Mike J. Taylor[1,2], and W. R. Pendleton Jr[1]

[1]Center for Atmospheric and Space Sciences and Physics Department, Utah State University, Logan, Utah, USA, [2]Physics Department, Utah State University, Logan, Utah, USA

Abstract The impacts of gravity wave (GW) on the thermal and dynamic characteristics within the mesosphere/lower thermosphere, especially on the atmospheric instabilities, are still not fully understood. In this paper, we conduct a comprehensive and detailed investigation on one GW breaking event during a collaborative campaign between the Utah State University Na lidar and the Advanced Mesospheric Temperature Mapper (AMTM) on 9 September 2012. The AMTM provides direct evidence of the GW breaking as well as the horizontal parameters of the GWs involved, while the Na lidar's full diurnal cycle observations are utilized to uncover the roles of tide and GWs in generating a dynamical instability layer. By studying the changes of the OH layer peak altitude, we located the wave breaking altitude as well as the significance of a 2 h wave that are essential to this instability formation. By reconstructing the mean fields, tidal and GW variations during the wave breaking event, we find that the large-amplitude GWs significantly changed the Brunt–Vaisala frequency square and the horizontal wind shear when superimposed on the tidal wind, producing a transient dynamic unstable region between 84 km and 87 km around 11:00 UT that caused a subsequent small-scale GW breaking.

1. Introduction

The gravity wave (GW) forcing and its related spectra within the mesosphere/lower thermosphere (MLT) are the key parameters for the understanding of energy and momentum transfers between the lower and middle atmosphere and the ionosphere. They have been known to drive the circulation and generate the counter intuitive cold summer and warm winter in the mesopause region [*Garcia and Solomon*, 1985], along with some irregularities in the ionosphere [*Liu and Vadas*, 2013]. Yet after decades of investigations, their characteristics and effects on the upper atmosphere are still not fully understood due to the GW's random spatial scales with their periods varying from a few minutes to several hours. Mainly generated in the troposphere by orographic, convection, and jet-front system, the GWs propagate upward with growing amplitude to compensate for the decrease of the air density due to conservation of the wave energy density during their propagation, before they reach the critical levels or become unstable and break [*Fritts and Alexander*, 2003]. It is also possible that the GW breaking can generate secondary waves within the breaking region [*Vadas et al.*, 2003; *Smith et al.*, 2013], affecting the atmosphere above MLT region. The wave breaking process deposits momentum into the mean flow field, causing mean flow acceleration in the wave propagation direction; changes the thermal structure; and generates turbulence around the breaking region.

Ground-based experimental studies have been playing the significant role in studying the GW dynamics and the associated atmospheric instabilities during the recent decades. However, single instrument only partially resolves the complex wave breaking process and the instability phenomenon. For example, the airglow measurement techniques like OH imaging [*Swenson and Mende*, 1994] can provide important horizontal wave structures information at high temporal resolution and capture the direct evidence of GW breaking and instability features like ripples, but it lacks vertical coverage of some key parameters, such as temperature and horizontal wind gradients, preventing a comprehensive investigation on this subject. On the other hand, lidar

and radar, especially narrowband sodium lidar [*Franke and Collins*, 2003; *Li et al.*, 2007a], are able to measure the temperature and wind vertical profiles, even the GW-induced horizontal momentum flux [*Acott et al.*, 2011], simultaneously with high resolution, and allow people to surgically carry out statistical studies on instability [*Zhao et al.*, 2003; *Li et al.*, 2005a]. However, without critical horizontal information about the GWs, such as horizontal phase speed and wavelength, it is also difficult to reveal the full spectrum of the wave breaking and the instability involved. Therefore, the combination of lidar or radar and airglow instruments is an extremely effective way to investigate the GW breaking events in details and has greatly advanced our understanding of GW dynamics in MLT region. *Fritts et al.* [1997] and *Hecht et al.* [1997] used Na lidar, imagers, and medium-frequency radar data combined with a 3-D model simulation to investigate the GW breaking and instability dynamics and found that the convective instability induced GW breaking and initiated ripples. *Yamada et al.* [2001] used data from an OH imager and meteor radar to report a GW breaking event and its transition to turbulence. Utilizing the combination of Na lidar and airglow instrument, *T. Li et al.* [2005] and *F. Li et al.* [2005b] investigated the ripples generated by dynamic and convective instabilities. *Ejiri et al.* [2009] reported a GW breaking case using two airglow instruments (O_2 imager and OH imager) and a meteor wind radar and concluded that the observed wave breaking was caused by critical level filtering. However, one of the major challenges in the GW dynamic studies is to distill the short-period GW perturbations and modulations from these experimental observations. Without the full diurnal cycle observation, it is highly difficult to precisely separate these short-period perturbations by GWs from the large-scale background, which mainly includes mean fields and the long-period modulations by tidal waves. This brings considerable uncertainties in the exploration of atmospheric instability and GW breaking, and the scenario becomes more pronounced in the MLT, where the tidal wave amplitude grows much larger than that in stratosphere and middle mesosphere.

In this paper we utilize the coordinated measurements from the Utah State University (USU) sodium lidar and a collocated Advanced Mesospheric Temperature Mapper (AMTM) to give a comprehensive investigation on a GW breaking event, and the associated instability occurred on the night of 9 September 2012. The lidar had been running 38 h continuously from 8 September to 9 September 2012 (UT day 252 to UT day 253), which allows us to separate the background and the GW perturbations, along with the characterization of some of the strong GWs. With the assistance of AMTM, we can not only determine the GW breaking level and uncover detailed mechanism of the wave breaking but also provide a clear description of the different atmospheric wave components' roles in initiating instability layers. Section 2 includes the description of the instruments involved during this campaign. In section 3, an overview of observation results from AMTM and Na lidar is presented. The detailed mechanism of GW breaking and instability layers, including the roles of the different components in initiating instabilities, followed by the GWs activity is presented in section 4. The summary and conclusion are in section 5.

2. Instrumentations

The USU Na lidar is a narrowband resonance fluorescence Doppler lidar system operating at the Na D2 line with a 120 MHz full-width half-maximum laser pulse bandwidth. The Na lidar is currently set up to probe the mesopause region simultaneously in three directions (north, east, and west) during the night and in two directions (north and east) during the daytime using a pair of Faraday filters [*Chen et al.*, 1996] to obtain high-resolution temperature and horizontal wind profiles, along with Na density profile. It provides the critical atmospheric information throughout a full diurnal cycle of observations of the mesopause region, such as tidal and planetary wave variations [*She et al.*, 2004; *Yuan et al.*, 2013] of all the lidar measurements.

The USU AMTM has been designed to measure the mesospheric OH (3,1) rotational temperatures over a large area, centered on the zenith. This instrument uses a fast (f:1) 120° field of view telecentric lens system designed and built at the Space Dynamics Laboratory, Logan, Utah, and 3 4″ narrow band (2.5–3 nm) filters centered on the P1(2), P1(4), and a nearby background region, mounted in temperature-stabilized filter wheel. The detector is an infrared camera fitted with a 320×256 pixel InGaAs sensor, thermoelectrically cooled to $-50°C$ to limit electronic noise, and controlled through a Universal Serial Bus port by a Windows computer. The exposure time for each filter was typically 10 s, giving precision temperature measurement (1–2 K) every ~30 s. This imager can operate in the presence of aurora and also acquires data under full moon conditions. Two of these instruments have been built so far. The first one has operated at the South Pole
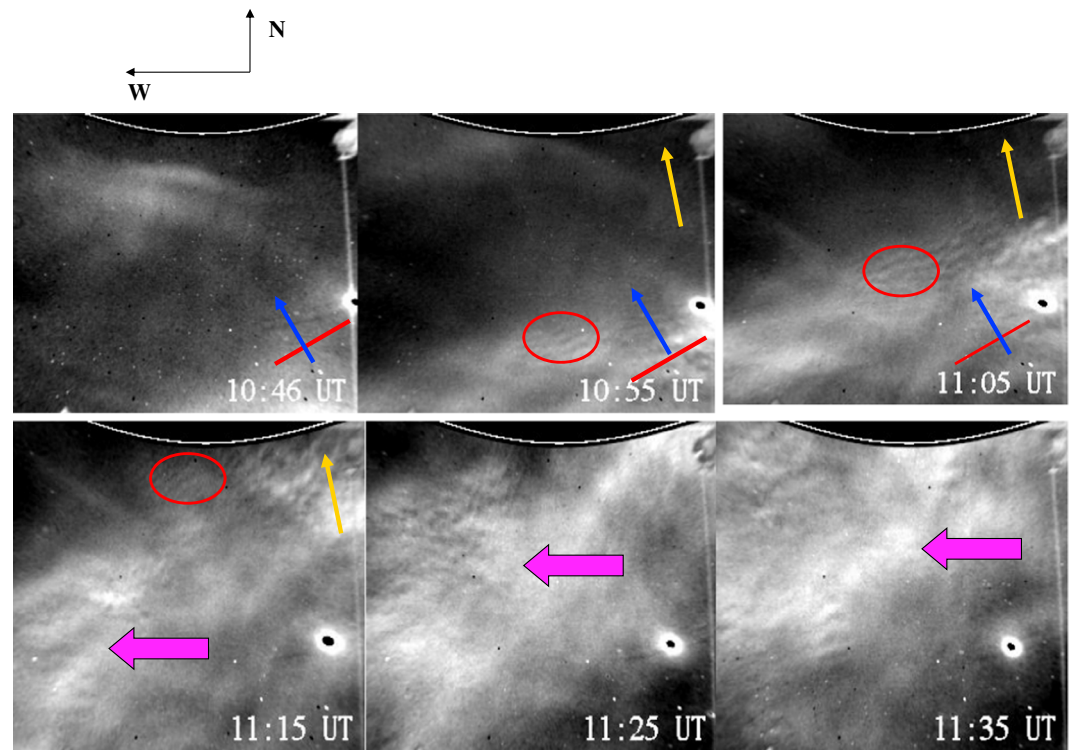
Figure 1. Time sequence of OH airglow images from 10:45 to 11:35 on 9 September 2012 for every 10 min. The up and left directions in each plot correspond to north and west. The red line stands for the wave before breaking, and the blue arrow is the propagation direction of the wave. The movement of ripple at 10:55, 11:05, and 11:15 are marked with red circle. The yellow arrow is the direction of horizontal wind. The breaking induced the turbulence feature intensified after 11:15 UT, which is marked by the pink arrow.

Station (90°S) since 2010 and the second one at the Arctic Lidar Observatory for Middle Atmosphere Research in northern Norway (69°N) since the winter 2010 and 2011. During the summer months, the later instrument has been returned to Utah for coordinated observations alongside the USU Na lidar (P.-D. Pautet, et al., An Advanced Mesospheric Temperature Mapper for high-latitude airglow studies, submitted to Applied Optics, 2014).

3. Observations

3.1. AMTM Observations

The AMTM was operating from 2:46 UT to 12:17 UT on 9 September 2012, and the data were processed with temporal resolution of 30 s, generating temperature uncertainty of 1 K. A small-scale wave that appeared from 10:45 UT to 11:05 UT in the mapper's field of view was propagating toward the azimuth 332° (±5°) relative to the north with an observed horizontal phase speed of 74 m/s(±5 m/s) and a horizontal wavelength of 20 km (±3 km). It had an observed period of 4.5 min and was seen breaking from 11:05 UT to 11:35 UT, as shown in Figure 1. The images of OH airglow emissions are presented in a 10 min time step from 10:45 UT to 11:35 UT in order to match with the temporal resolution applied to Na lidar data analysis. The red line marks the wavefront before the breaking, and the blue arrow indicates the wave propagation direction. This wave propagated into the AMTM's field of view from the bottom right corner near 10:46 UT and started to lose its waveform between 10:55 UT and 11:05 UT. It is worth noticing that a ripple-like feature (marked by red circle), perpendicular to the wave propagation direction, showed up at 10:55 UT ahead of the wavefront and was traveling toward north until it disappeared around 11:15 UT. After that, the wave breaking became much vigorous and completely transformed into turbulence feature (marked by the pink arrow). This turbulence feature eventually covered almost the entire field of view of the AMTM (180 km × 144 km).
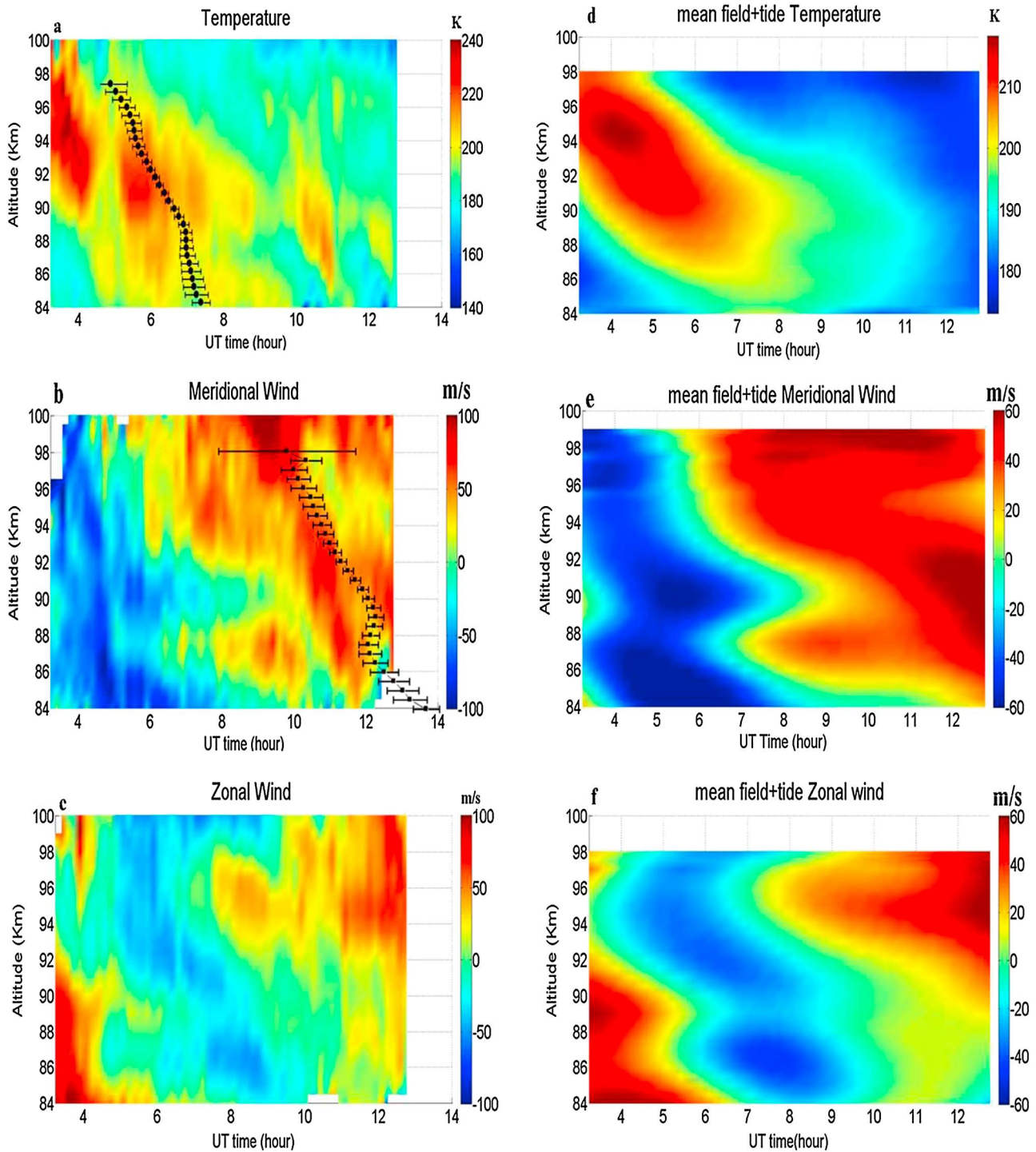
Figure 2. Contours of the lidar-observed (a) temperature, (b) meridional wind, and (c) zonal wind observations on the night of 9 September 2012 by USU Na lidar in the mesopause region (84–100 km), along with the phase profile of semidiurnal tide (black point and line). The phase profile of semidiurnal tide of zonal wind field is out of the night's temporal range. The reconstructed background (d) temperature, (e) meridional wind, and (f) zonal wind are deduced by utilizing the mean fields and tidal parameters deduced from the linear square harmonic fitting algorithm.

Hecht [2004] summarized the atmospheric instability-induced ripple in the airglow measurements and pointed out that the alignment between the ripple and bands in OH airglow direction has distinct feature due to different associated instabilities. Convective instability induces ripples that are perpendicular to the OH bands, while dynamic instability generates ripples that are aligned parallel to the wave bands. Such features

during atmospheric instability in the mesopause region are expected and have been reported by previous studies [*T. Li et al.*, 2005; *F. Li et al.*, 2005b]. We have a detailed discussion on this instability formation based upon the lidar's temperature and wind measurements in section 4.2. Apart from the direct evidence of GW breaking, the AMTM observed several ripple features during the night, implying the possible existence of other instabilities during that night.

3.2. Na Lidar Observations

The contour plots of the Na lidar-observed temperature and wind measurements are presented in the left column of Figure 2. Here the lidar data were processed with 10 min and 2 km temporal and spatial resolutions, respectively. From the figure, it can be seen that the lidar-measured temperature and meridional wind are clearly dominated by a large-scale, coherent oscillation with a downward phase progression of 3 km/h, most likely a semidiurnal tide in nature, while the zonal wind structure shows no clear tidal structure at all. Also in these contours of lidar observations, semidiurnal tidal phase profile, which marks the time of the tidal maximum modulation, is plotted for each lidar altitude. The absence of the zonal wind tidal maximum is mainly due to the revealed tidal wave dispersion relationship [*Yuan et al.*, 2008], which indicates the zonal wind semidiurnal maximum mostly occurs in the late morning and late afternoon in this midlatitude mesopause region. Therefore, it is not expected to play a significant role in the nighttime observations. Here the tidal results are based upon the outputs of a linear least squares fitting algorithm that is applied on the lidar diurnal measurements. During the AMTM-observed wave breaking period, a strong temperature enhancement that occurred after 10:00 UT was observed by the Na lidar within the altitude range of OH layer. The temperature enhancement reached about 215 K around 11:00 UT near 87 km, which appeared to be part of a 2 h wave modulation. This enhancement was well separated from the tidal feature between 84 km and 90 km during the first half of the night, and in excellent agreement with the AMTM-observed OH rotational temperature modulation during the same period, which shows a similar 2 h wave feature as well. Also from the Figure 2, the temperature enhancement was accompanied by an apparent large wind shear (~40 m/s/km) in the meridional wind around 11:00 UT at the altitude range of 85–88 km, which was superimposed on top of the meridional semidiurnal maxima. During the same time, however, the zonal wind did not show much abnormal variation.

Based on the high-resolution Na lidar data, we have calculated the vertical gradients of the zonal and meridional wind, as well as the Brunt–Vaisala frequency square (N^2) and the Richardson number (Ri) using the following equations:

$$N^2 = \frac{g}{T}\left(\frac{dT}{dz} + \frac{g}{C_p}\right) \tag{1}$$

$$Ri = \frac{N^2}{\left(\frac{dU}{dz}\right)^2 + \left(\frac{dV}{dz}\right)^2} \tag{2}$$

where $g = 9.5 * 10^\wedge - 3$ m/s^2 is the gravitational acceleration at the altitude of mesopause region. C_P is the per unit mass specific heat per unit mass at constant pressure, and T is the temperature. In the MLT region, the lapse rate is $\frac{g}{C_P} = 9.5$ K/km. The $\frac{dT}{dz}, \frac{dU}{dz}$, and $\frac{dV}{dz}$ are the vertical temperature gradient, shears of the zonal wind, and meridional wind, respectively.

The variations of horizontal wind gradient during the latter part of night 253 are shown in the contour plots of Figure 3a, along with those of N^2 and Ri. A GW breaks when propagating into either unstable region ($N^2 < 0$ for convective instability or $0 < Ri < 0.25$ for dynamic instability) or when reaching its critical level (CL) (where the horizontal wind speed matches the wave's horizontal phase speed in its propagating direction [*Fritts and Alexander*, 2003]). Transient instabilities can be induced by the superposition of a small-scale GW on the tidal-modulated background, thus triggering wave breaking.

During the second half of night 253, there was two enhancements of N^2 (Figure 3b) at altitude range of 85–89 km that were roughly 2 h apart. The horizontal wind shear was also strongly modulated by a strong 2 h wave after 9:30 UT with its maximum lagging that of N^2. But the wave's downward progression feature was largely disturbed after 11:30 UT below 87 km. In Figure 3c, the dynamic instability between 11:00 UT and 11:30 UT occurred near the maximum of horizontal wind shear (~40 m/s/km) near 86 km. Therefore, the 2 h GW played an important role in the atmospheric variations after 9:30 UT in the altitude range of 84–90 km.
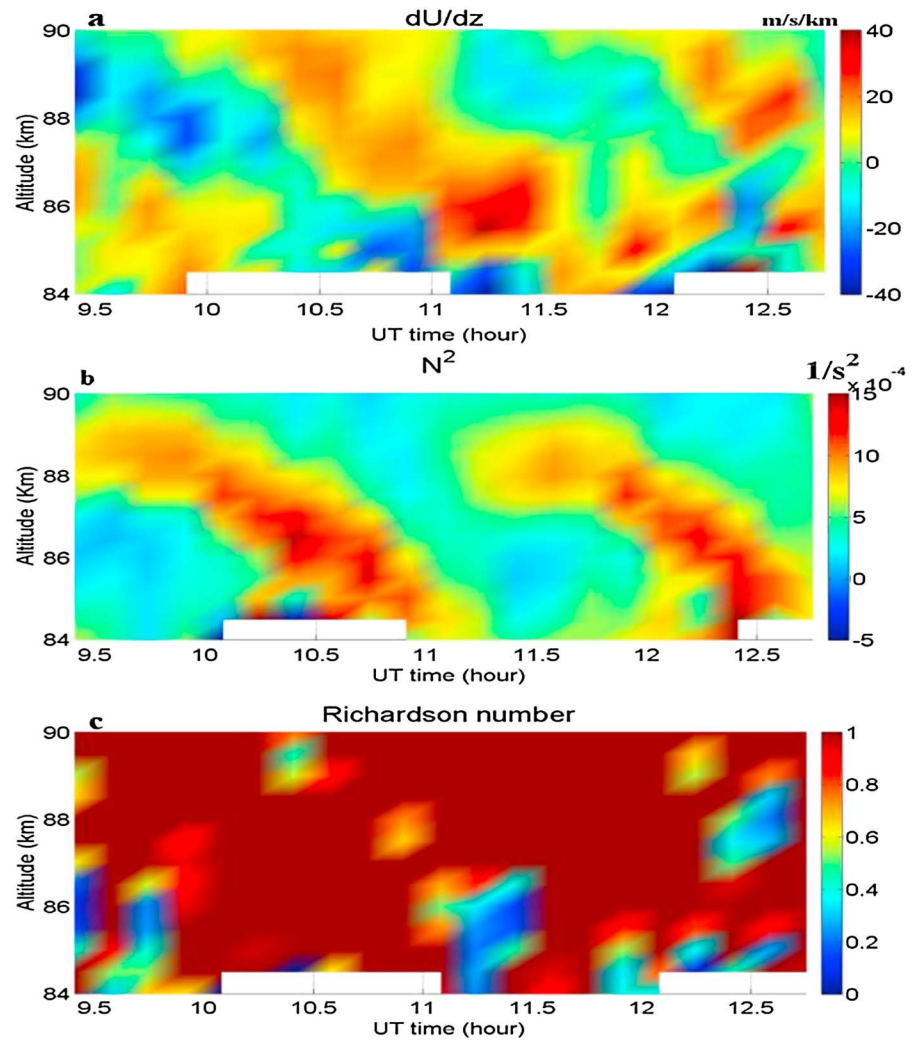
Figure 3. Time-altitude contours of (a) horizontal wind shear, (b) Brunt–Vaisala frequency (N^2), and (c) Richardson number (*Ri*) from 84 to 90 km and from 9:25 to 12:45 UT.

This 2 h wave was also found staying active throughout the rest of the lidar observation below 92 km and can be clearly seen in the lidar's subsequent daytime observations.

4. Discussions and Analysis

4.1. The Gravity Wave Breaking Altitude and Background Stability (11:05 UT–11:35 UT)

Since the AMTM covers the whole range of hydroxyl layer, to locate the precise GW breaking altitude range, the OH layer peak altitude during the breaking event has to be calculated to account for the layer's vertical fluctuations, mainly due to the modulations of tidal waves and large-scale gravity waves. This is achieved by comparing height-weighted lidar temperatures with the concurrent AMTM temperature measurements following the method presented by *Zhao et al.* [2005]. Basically, at each time point, the lidar temperature is height weighted using a 9 km full width at half maximum Gaussian profile centered at each assumed central heights between 82 and 92 km (in 0.1 km step). Such Gaussian profile is found to be close to the OH layer thickness and shape [*Baker and Stair*, 1988; *Yee et al.*, 1997]. For altitudes below 90 km, the Gaussian profile was truncated at altitudes where the lidar temperature errors increase due to the lower sodium density (lower signal level) at the edge of the sodium layer. The height-weighted lidar temperatures at different assumed central heights were then compared with the AMTM temperature values at the corresponding time. The assumed altitude with the minimum difference between the weighted lidar temperature and AMTM
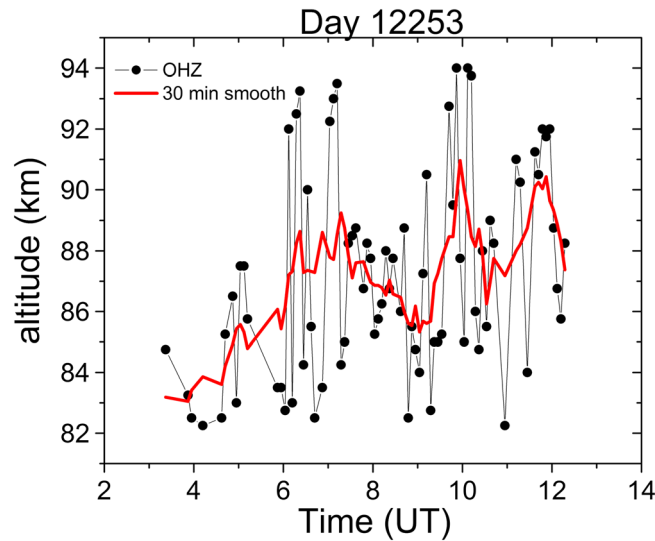
Figure 4. The variations of OH layer peak altitude on the night of 9 September. The black dots in the figure stand for the peak altitude deduced from the lidar-observed temperatures with a 5 min temporal resolution. The red line is in a 30 min smoothing.

temperature was selected as the OH peak height. Figure 4 shows the results of this algorithm during the night. The results of high temporal resolution, using 5 min lidar profiles, show dramatic oscillations of the OH peak altitude, while those of the 30 min smoothing are quite helpful for locating long the period wave's modulations. Based on the 30 min smoothing results, it can be clearly seen that the peak altitude of the hydroxyl layer varied significantly during the night from around 83 km at the beginning of the observation to above 90 km near 12:00 UT. Between 3:00 UT and 6:00 UT, the peak of OH layer moved up 1.5 km/h. From 7:00 UT to 12:30 UT, the OH peak altitude was clearly oscillating with a 2 h wave feature with two peaks at 10:00 UT and 12:00 UT. The average amplitude of the oscillation is estimated to be less than 2 km.

Intriguingly, such overall upward OH layer fluctuations throughout the night are very different from those of the previous similar studies [*Reisin and Scheer*, 1996; *Hecht et al.*, 1998; *Taylor et al.*, 1999; *Pendleton et al.*, 2000; *Zhao et al.*, 2005], which presented a clear downward trend due to either a diurnal tide or a tide superimposed with a short-period GW. From the determined fluctuation of OH peak altitude, we can see that this 2 h GW activity was quite strong during that night from 10:00 UT to 12:00 UT and dominated variations of the OH layer altitude. During the time of the wave breaking (11:05 UT to 11:35 UT), the OH peak was pushed upward from 87 to near 90 km, and this 2 h wave feature is in agreement with the Na lidar temperature results during the second half of the night. Therefore, to fully reveal the wave breaking mechanism, we focus our investigations on the lidar temperature and wind measurements within this altitude range surrounding this breaking event.

From Figure 3b, N^2 is mostly larger than 0 from 9:25 UT to 12:45 UT, implicating that the atmosphere was convectively stable and the observed GW breaking was unlikely triggered by convective instability. To have a good estimation of the GW's critical level, the background temperature and horizontal wind need to be precisely measured and calculated. We define this background as the large-scale variations due to the combination of mean field and the tidal waves. Here a least squares fitting [*Yuan et al.*, 2006; *Yuan et al.*, 2010] is applied to the hourly lidar measurements at each altitude of this 38 h continuous data set:

$$S = A_0 + \sum_{i=1}^{4} A_i \cos\left(\frac{2\pi i}{24}t - \varphi_i\right) \qquad (3)$$

where S can be the wind or the temperature, A_0 the mean field, $i = 1$ for the diurnal tide, $i = 2$ for the semidiurnal tide, $i = 3$ for the terdiurnal tide, $i = 4$ for the quardiurnal tide, and φ_i represents the tidal phase for the ith tidal component.

Utilizing the fitting results, the contour plots of the reconstructed background temperature, meridional wind, and zonal wind for every 10 min on that night are shown in Figures 2d–2f, respectively. These reconstructed background wind results are then utilized to calculate the horizontal velocity projected in the GW propagation direction (334° relative to the north). Due to the high horizontal phase speed (74 m/s) of the GW before its breaking, which is much larger than the background horizontal wind projected onto the direction of the GW, its CL was not likely formed within the hydroxyl layer. On the other hand, as shown in Figure 3c, there was a dynamically unstable region from 11:00 to 11:30 UT between 84 and 87 km, which overlaps the time and altitude ranges of the AMTM-observed GW breaking event in Figure 1. This, along with the AMTM captured ripple feature during the same time, indicates dynamic instability's essential role in this wave breaking event.
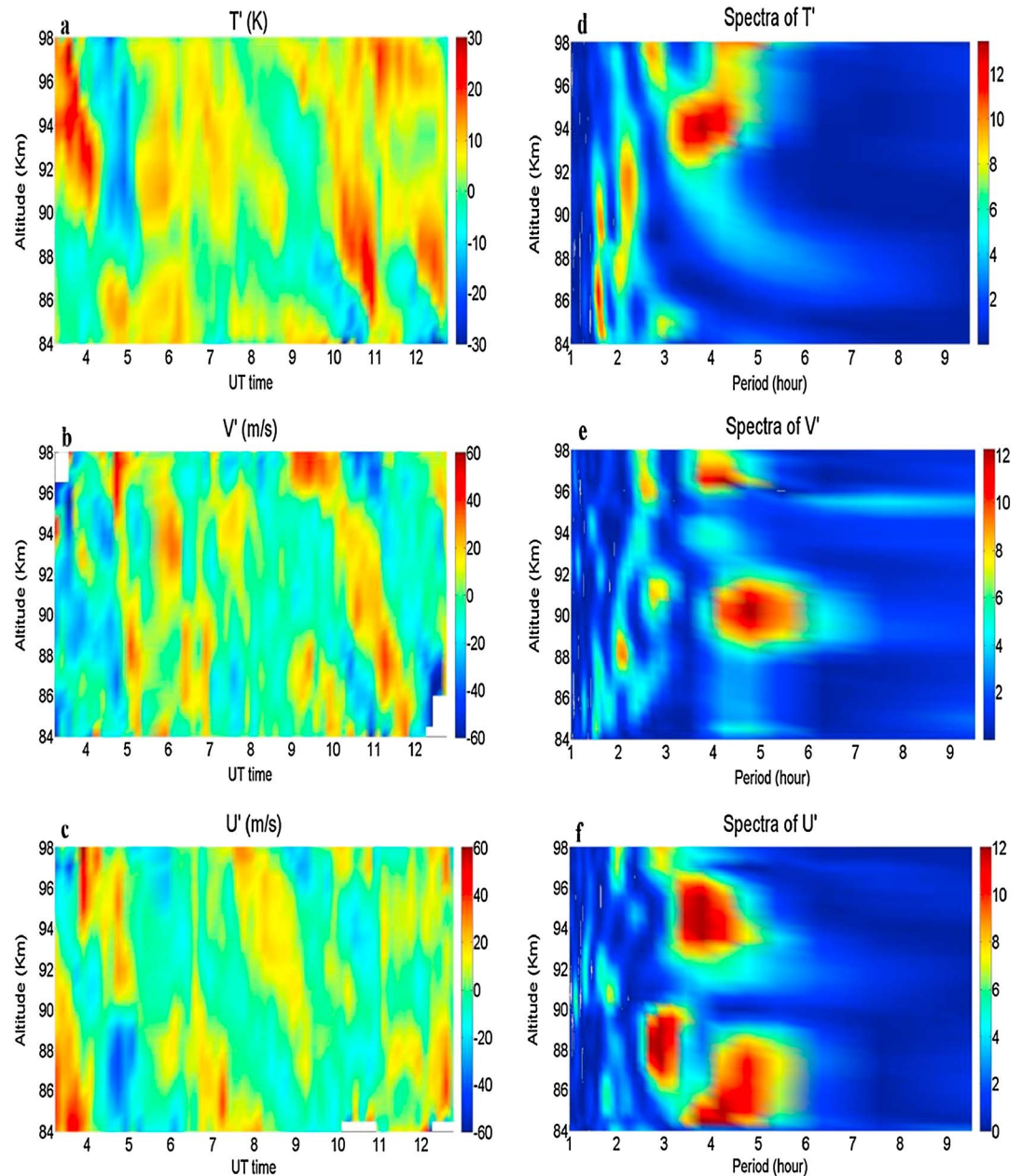
Figure 5. The lidar-observed short-period GW perturbations by subtracting the mean field and tidal wave's modulations: (a) temperature perturbations, (b) meridional wind, and (c) zonal wind perturbations (84–98 km) on 9 September. (d–f) The corresponding spectra for these perturbations (from 84 km to 98 km).

4.2. Dynamic Instability

In this section, we investigate the formation of the above mentioned dynamic instability that most likely triggered the small-scale GW breaking. To discover the dominant GW components on the later part of night 253, the GW perturbations (Figures 5a–5c) are obtained by subtracting the reconstructed background from the original lidar measurements (10 min temporal resolution). From the figures, the 2 h perturbations are clearly visible in temperature and meridional wind field but much weaker in the zonal wind field. It is worth noticing that the meridional wind perturbation appears to be lagging the temperature perturbation by roughly 30 min. This is a good agreement with the polarization relationship of the medium-frequency GWs [*Fritts and Alexander*, 2003], which implies that the temperature perturbation should lead the horizontal wind perturbation (in this case the horizontal wind is mostly in the meridional direction) by $\pi/2$. The spectra of
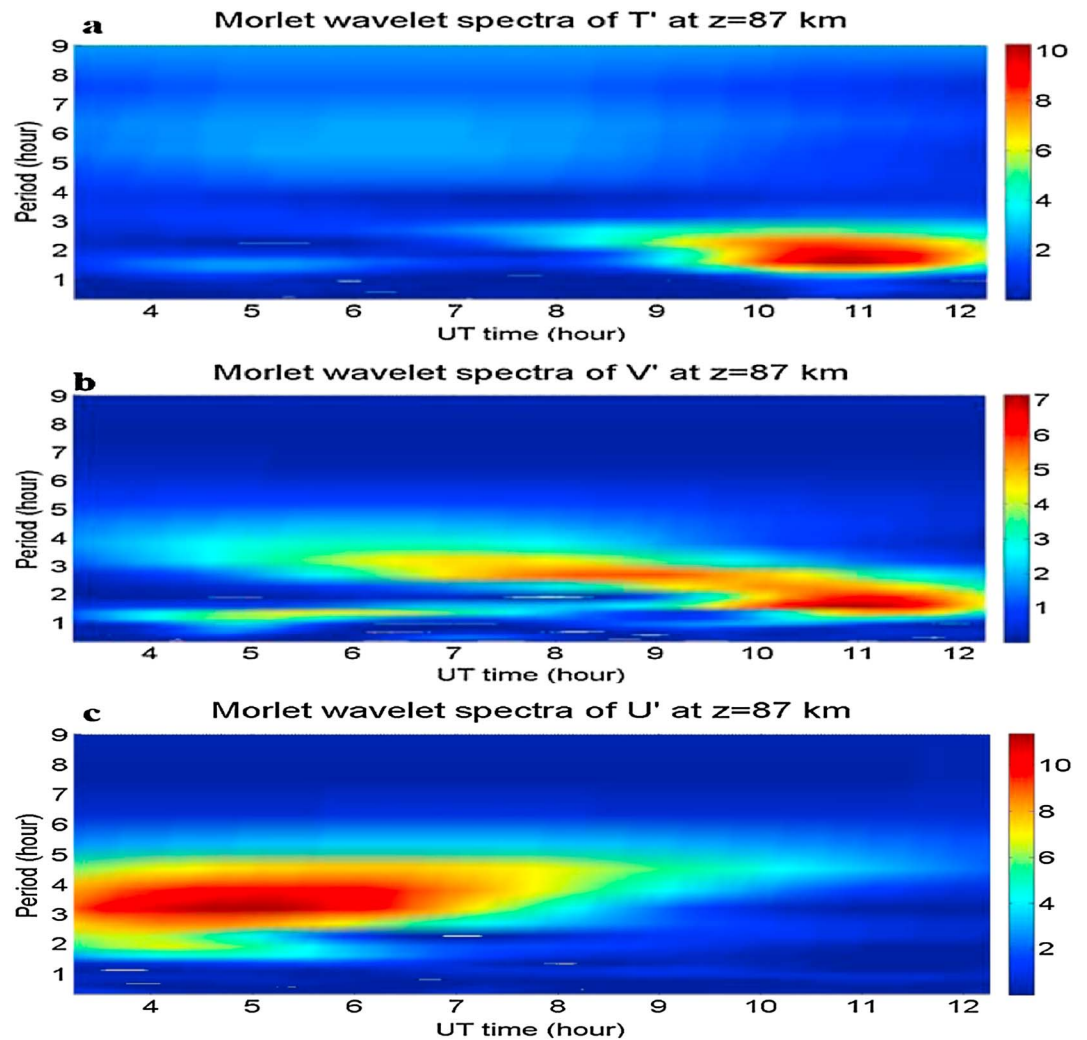
Figure 6. The variations of the amplitude of Morlet wavelet spectra at 87 km for the lidar measurements of (a) temperature perturbation, (b) meridional wind, and (c) zonal wind perturbations.

theGWs perturbations for the whole night in temperature and horizontal wind fields are calculated and shown in Figures 5d–5f, which show the existence of four large-scale GWs during that night: a 1.5 h GW and a 2 h GW are clearly visible from 84 to 92 km in temperature and meridional wind field; a 3 h GW is dominant from 89 to 91 km, 96 to 98 km in meridional wind field, and 87 to 90 km in zonal wind field; and a 4 h period GW is from 88 to 91 km, 95 to 98 km in meridional wind field, and 84 to 89 km and 93 to 97 km in zonal wind field. The 1.5 h and 2 h GWs both have very strong components in the meridional wind field, while the 3 h and 4 h GWs are pronounced in zonal wind field. To determine the variations of the dominant GWs during different part of the night within the hydroxyl layer, we also calculated the Morlet wavelet spectra of T, V, and U [*Torrence and Compo*, 1998]. Looking at the Morlet wavelet spectra at 87 km in Figure 6, it is quite obvious that different GW component dominated different part of the night: the temperature and meridional wind fields are dominated by GWs with periods between 1.5 and 3 h during the second half of the night, especially the dominance of the 2 h modulation from 10:00 UT to 12:00 UT, while the zonal wind field experienced strong GW modulations with periods around 3–4 h during the first half of the night.

Through this spectrum analysis, we can further reconstruct the temperature and wind variations to include these major GW's modulations and characterize the roles of these major GWs in forming the instabilities that induced the observed wave breaking. As shown in Figure 6, from the Morlet wavelet spectrum, the 1.5 h and 2 h GWs are the main component of perturbations in the second half of the night. Therefore, we fitted the lidar-measured temperature and wind perturbations with 1.5 h and 2 h GWs together within a 2 h sliding
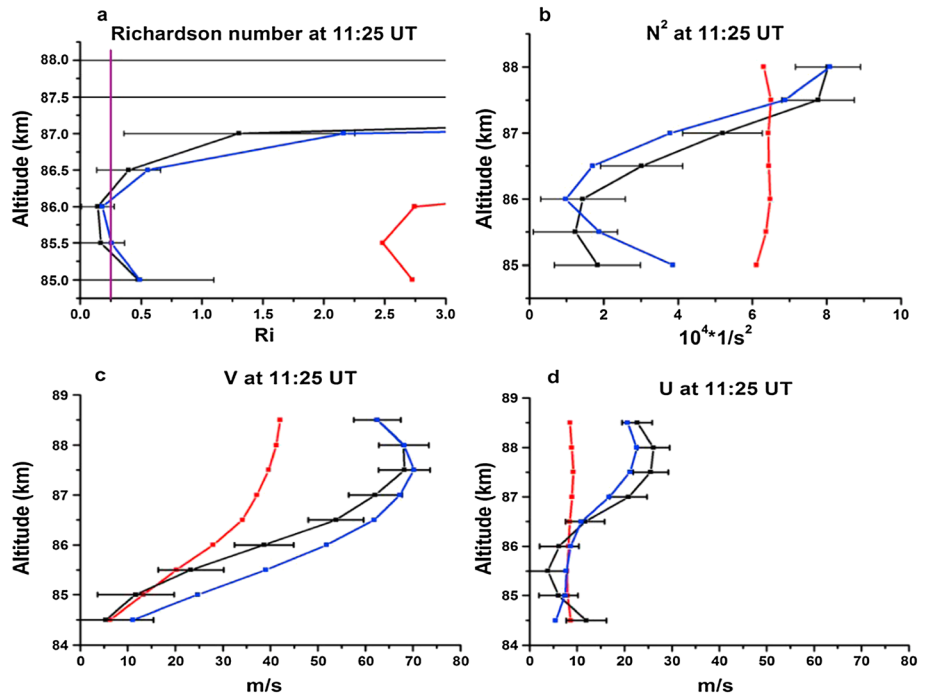
Figure 7. The profiles at 11:25 UT of (a) Richardson number profiles (Ri), (b) profiles of Brunt–Vaisala frequency square (N^2), (c) meridional wind, and (d) zonal wind. The black lines correspond to the values deduced from the original lidar data and the associated error. The red lines are for the values derived from the reconstructed background data, and the blue one is derived from the combination of the reconstructed background with reconstructed gravity waves. The purple line in Figure 7a stands for $Ri = 0.25$.

window. The window moves at 10 min step on the lidar perturbation data between 8:45 and 12:45 UT. At each step, these GW's amplitudes and phases can be achieved, and the GW's modulations can be reconstructed. Then we combined the already achieved reconstructed background with these reconstructed GW's perturbations to simulate the temperature and horizontal wind variations, as well as the Ri, during the wave breaking period. Figure 7a shows the Ri profiles at 11:25 UT that are associated with the observed instability layer below 90 km. These profiles include the Ri profile directly calculated through lidar measurements, the Ri calculated through the reconstructed background alone, and the Ri profile deduced from the combination of the reconstructed background and the reconstructed major GWs modulations. From this plot, we can clearly see that the Ri profile calculated from the combination of the reconstructed background with the reconstructed GWs is very similar to the Ri calculated directly from the lidar profiles, indicating the success of the characterizations of the background and the GW's modulations in this algorithm. To further investigate the GW's impacts on the dynamic condition during this wave breaking event, we applied the same algorithm and present profiles of N^2, the meridional wind (V), and the zonal wind (U) at 11:25 UT as well in Figure 7.

Looking at Figure 7a, the Ri calculated directly from the lidar measurements, termed as the observed Ri, and the Ri derived from combination of the background with the reconstructed GWs, termed as the reconstructed Ri, are both near or less than 0.25 at 85.5 km and 86 km, while the Ri calculated from the reconstructed background alone, termed as the background Ri, are all much larger than 0.25, indicating that the large-scale background is fairly stable. Also from the figure, the background N^2 does not change that much from 85 to 88 km and is very different to the observed N^2, while the reconstructed N^2 profile is almost parallel to the observed N^2. The figure also shows that when the major GWs were included, the N^2 values dropped significantly from $6.367 \times 10^{-4}/s^2$ and $6.468 \times 10^{-4}/s^2$ to $1.88 \times 10^{-4}/s^2$ and $0.97 \times 10^{-4}/s^2$, respectively, near the dynamic unstable region. However, within the range of the uncertainty, the atmosphere is still convectively stable near the wave breaking level.

As far as the wind shear, when only the background is taken into account, the meridional wind shear was 14.57 m/s/km and 13.9 m/s/km at 85.5 km and 86 km. It increased to 27.05 m/s/km and 22.78 m/s/km once

Direction of mean wind, tidal wind and 2-hour GW at 11:15 UT,87km
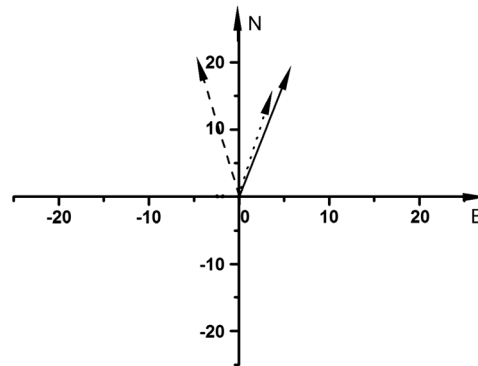
Figure 8. The mean horizontal wind (solid arrow), the 2 h wave propagation direction (dashed arrow), and the tidal wind direction (dotted arrow) at breaking time 11:15 UT, 87 km.

the major GWs were introduced in the reconstruction. The zonal wind shear was less than 1 m/s/km and therefore is not expected to contribute very much to the total wind shear and the associated Ri. It is also worth noticing that in both wind shears, the differences caused by GWs above 87 km are much larger than those below, most likely due to the growing of the GW's amplitude. Based upon the above detailed discussion on the GW impacts on N^2 and wind shear value, it is clear that large-amplitude GWs played a significant role in the evolution of N^2 and Ri and the associated atmosphere instability locally during short time scale.

Looking back to the Morlet wavelet spectra at 87 km in Figure 6, the 1.5 h and 2 h GWs were very consistent and are the dominant GW components after 10:00 UT in both the temperature and meridional perturbations fields, while these GWs are fairly weak in zonal wind field. Therefore, these two GWs played crucial roles in the dynamic instability formed between 10:00 and 11:30 UT, which induced the breaking of the small-scale GW. There was another significant dynamic instability region observed between 7:30 UT and 09:00 UT during the same night between 91 km and 93 km, also due to the combination of background and a large-amplitude GW, likely an inertia GW with fairly long, short vertical wavelength. However, it is found that, in that case, the dominant GW component was the 4 h GW and it impacted mostly in the zonal direction. Unfortunately, this region is above hydroxyl layer; thus, the GW's behaviors within this dynamic instability layer are unable to be fully measured.

4.3. The 2 h Gravity Wave

The harmonic fitting shows that the 1.5 h modulation is relatively weaker compared to the 2 h wave. Thus, the 2 h wave becomes particularly important in this study. This is also because this GW was observed by both the Na lidar and the AMTM and played a significant role in the observed wave breaking process. The comprehensive coverage in both horizontal and vertical direction provides an opportunity for a detailed study of full characters of this wave. As shown by the Figure 3a, it generated very large wind shear in the meridional direction when superimposed on top of the semidiurnal tide and decreased Ri to near or less than 0.25, thus initiated the breaking of a small-scale GW around 11:05 UT. Figure 8 presents a direct view of the directions and magnitudes of the mean wind, the total tidal wind, and the 2 h wave wind at 87 km when the instability occurred. It shows that the tidal wind aligned with the mean horizontal wind fairly well, while the horizontal wind component of the 2 h wave was also in the similar direction to the tidal wind. Combined with the lidar horizontal wind measurement, we decide that its intrinsic period was 2.45 h with intrinsic phase speed of 148.72 m/s during wave breaking time. The AMTM data revealed that it had an observed horizontal phase speed of 180 m/s toward north-northwest, horizontal wavelength of 1230 km, which is in the similar magnitude of the wavelength of inertial gravity waves (IGWs). Through the fitting parameters that we deduced, we estimate its vertical phase speed of 2.4 m/s, associate with 17.3 km vertical wavelength, which is in agreement with the magnitude of the downward progression feature in the lidar's GW perturbation observations of Figures 5a and 5b. This wavelength is also in agreement with the one associated with the IGW that had been reported at the same latitude in Fort Collins by *Li et al.* [2007b], which was 15–20 km below 97 km and dropped quickly to 0 around 102 km, due to the filtering by its critical level. However, in this case, the 2 h GW here was still propagating beyond 98 km, most likely because of its fast horizontal phase speed. It is also found that during the wave breaking process, its amplitude was 15 K in temperature field and >20 m/s in meridional wind field during wave breaking time around 87 km. Its zonal wind amplitude is found to be ~5.7 m/s at the same altitude.

Based on the GW polarization relationship under medium-frequency approximation [*Fritts and Alexander*, 2003], $\widetilde{w} = \left|\frac{k_h}{m}\right| \widetilde{u}_h$, where $\widetilde{w}$ and $\widetilde{u}_h$ are the vertical wind perturbation and horizontal wind perturbation, respectively. From the deduced horizontal wind amplitude and the above calculated wavelength, we estimate the vertical wind perturbation to be roughly 1.27 km/h and lead the horizontal wind perturbation by

180°. These results are in accordance with the observed oscillations of the hydroxyl layer's peak altitude presented in Figure 4 and described in section 4.1. Based upon another polarization relationship of the medium-frequency wave [*Fritts and Alexander*, 2003, equation (26)], we have the relationship between the meridional wind perturbations and the zonal wind perturbations without dissipation as

$$\widetilde{u} = \left(\frac{i\hat{\omega}k - fl}{i\hat{\omega}l + fk}\right)\widetilde{v} \tag{4}$$

A further simplification ($N >> \hat{\omega} >> f$, and the wave propagation direction is 345°, so $l > k$) gives $\widetilde{u} \approx \frac{k}{l}\widetilde{v}$, where k and l are the zonal and meridional wave numbers, respectively. From the AMTM observation, this ratio is ~0.27, which gives the zonal amplitude of ~5.4 m/s. This is in excellent agreement with the lidar-observed zonal wind amplitude of this 2 h wave mentioned above and explains why the meridional component is much larger than the zonal component. This simplified polarization relationship also implies that the zonal wind component and meridional wind component are mostly in phase with each other, which is also highly consistent with the lidar-observed phase relationship (now shown) of the 2 h wave. Such good agreement with the medium-frequency GW for none dissipation scheme may imply that this 2 h wave experienced little dissipation during this transient dynamic instability.

5. Summary and Conclusion

In this study, to understand the effects of large-amplitude gravity wave on the atmosphere instability within the hydroxyl layer, we have conducted a comprehensive and detailed investigation on a GW breaking event captured on the later part of the night on 9 September 2012 by the USU AMTM. Using both the USU Na lidar and AMTM temperature results, we are able to calculate the variations of the OH layer's peak altitude throughout the night and thus reveal that this wave breaking event was taking place near 87 km. The observations show that wave breaking occurred when a small-scale GW propagated into a dynamical unstable region formed around 11:00 UT and started to break immediately.

Benefited from the lidar's full diurnal cycle observation, we are able to confidently separate the GW-induced perturbations and slowly changing large-scale background, which consists of mean fields and tidal wave modulations. This enables us to evaluate their individual roles in the formation of the atmosphere instability. The spectrum analysis uncovers that there were several active large-amplitude GWs during the night and a 2 h wave were clearly dominant during wave breaking process. The large-amplitude 2 h GW was also observed in OH rotational temperature and the variations of the OH layer's peak altitude by the AMTM. It had an observed horizontal phase speed of 180 m/s, horizontal wavelength 1230 km, vertical phase speed of 2.4 m/s, and vertical wavelength 17.3 km. It maintained its propagation form within the mesopause region and beyond 98 km mainly due to its fast horizontal phase speed. During the small-scale GW breaking process, its amplitude reached to ~15 K in temperature and ~20 m/s in meridional wind, while its modulation of zonal wind was quite weak. The transient dynamically unstable region was thus formed by the superposition of this large-amplitude GWs and meridional wind semidiurnal tidal maximum in the early morning. In addition, the major GWs induced a decrease of the N^2 value of 80%, which catalyzed the formation of the dynamic instability. The observed polarization relationship of this 2 h wave agrees extremely well to that of the medium-frequency GW under none-dissipation scheme, implying that the 2 h wave dissipated very little during the observed instability.

Overall, this study has discussed a small-scale GW breaking event, when it was propagating into a transient dynamic instability layer, which is formed by the combination effects of large-amplitude GWs and the tidal wave-modulated large-scale background. The study also precisely decides the roles of background and GWs in this wave breaking event, which concludes that it is the large-amplitude GWs that pushed the region within the hydroxyl layer into dynamic unstable momentarily. This study also demonstrates the capability of the coordinated observations between AMTM and Na Doppler/temperature lidar for detailed and comprehensive investigations on GW dynamics within MLT.

References

Acott, P. E., C. Y. She, D. A. Krueger, Z. Yan, T. Yuan, J. Yue, and S. Harrell (2011), Observed nocturnal gravity wave variances and zonal momentum flux in midlatitude mesopause region over Fort Collins, Colorado, *J. Atmos. Sol. Terr. Phys.*, 73, 449–456.
Baker, D. J., and A. T. Stair Jr. (1988), Rocket experiments of the altitude distributions of the hydroxyl airglow, *Phys. Scr.*, 37, 611–622.

Chen, H., M. A. White, D. A. Krueger, and C. Y. She (1996), Daytime mesopause temperature measurements using a sodium-vapor dispersive Faraday filter in lidar receiver, *Opt. Lett.*, *21*, 1003–1005, doi:10.1364/OL.21.001093.

Ejiri, M. K., M. J. Taylor, T. Nakamura, and S. J. Franke (2009), Critical level interaction of a gravity wave with background winds driven by a large-scale wave perturbation, *J. Geophys. Res.*, *114*, D18117, doi:10.1029/2008JD011381.

Franke, P. M., and R. L. Collins, (2003) Evidence of gravity wave breaking in lidar data from the mesopause region, *Geophys. Res. Lett.*, *30*(4), 1155, doi:10.1029/2001GL014477.

Fritts, D. C., and M. J. Alexander (2003), Gravity wave dynamics and effects in the middle atmosphere, *Rev. Geophys.*, *41*(1), 1003, doi:10.1029/2001RG000106.

Fritts, D. C., J. R. Isler, J. H. Hecht, R. L. Walterscheid, and O. Andreassen (1997), Wave breaking signatures in sodium densities and OH nightglow: 2. Simulation of wave and instability structures, *J. Geophys. Res.*, *102*, 6669–6684, doi:10.1029/96JD01902.

Garcia, R. R., and S. Solomon (1985), The effect of breaking gravity waves on the dynamics and chemical composition of the mesosphere and lower thermosphere, *J. Geophys. Res.*, *90*, 3850–3868, doi:10.1029/JD090iD02p03850.

Hecht, J. H. (2004), Instability layers and airglow imaging, *Rev. Geophys.*, *42*, RG1001, doi:10.1029/2003RG000131.

Hecht, J. H., R. L. Walterscheid, D. C. Fritts, J. R. Isler, D. C. Senft, C. S. Gardner, and S. J. Franke (1997), Wave breaking signatures in OH airglow and sodium densities and temperature: 1. Airglow imaging, Na lidar, and MF radar observations, *J. Geophys. Res.*, *102*, 6655–6668, doi:10.1029/96JD02619.

Hecht, J. H., et al. (1998), A comparison of atmospheric tides inferred from observations at the mesopause during ALOHA–93 with the model predictions of the TIME-GCM, *J. Geophys. Res.*, *103*, 6307–6321, doi:10.1029/97JD03377.

Li, F., A. Z. Liu, and G. R. Swenson (2005a), Characteristics of instabilities in the mesopause region over Maui, Hawaii, *J. Geophys. Res.*, *110*, D09S12, doi:10.1029/2004JD005097.

Li, F., A. Z. Liu, G. R. Swenson, J. H. Hecht, and W. A. Robinson (2005b), Observations of gravity wave breakdown into ripples associated with dynamical instabilities, *J. Geophys. Res.*, *110*, D09S11, doi:10.1029/2004JD004849.

Li, T., C. Y. She, B. P. Williams, T. Yuan, R. L. Collins, L. M. Kieffaber, and A. W. Peterson (2005), Concurrent OH imager and sodium temperature/wind lidar observation of localized ripples over northern Colorado, *J. Geophys. Res.*, *110*, D13110, doi:10.1029/2004JD004885.

Li, T., C. Y. She, H.-L. Liu, and M. T. Montgomery (2007a), Evidence of a gravity wave breaking event and the estimation of wave characteristics from sodium lidar observation over Fort Collins, CO (41°N, 105°W), *Geophys. Res. Lett.*, *34*, L05815, doi:10.1029/2006GL028988.

Li, T., C.-Y. She, H.-L. Liu, T. Leblanc, and I. S. McDermid (2007b), Sodium lidar–observed strong inertia-gravity wave activities in the mesopause region over Fort Collins, Colorado (41°N, 105°W), *J. Geophys. Res.*, *112*, D22104, doi:10.1029/2007JD008681.

Liu, H.-L., and S. L. Vadas (2013), Large-scale ionospheric disturbances due to the dissipation of convectively generated gravity waves over Brazil, *J. Geophys. Res. Space Phys.*, *118*, 2419–2427, doi:10.1002/jgra.50244.

Pendleton, W. R., Jr., M. J. Taylor, and L. C. Gardner (2000), Terdiurnal oscillations in OH Meinel rotational temperatures for fall conditions at northern midlatitude sites, *Geophys. Res. Lett.*, *27*, 1799–1802, doi:10.1029/2000GL003744.

Reisin, E. R., and J. Scheer (1996), Characteristics of atmospheric waves in the tidal period range derived from zenith observations of O2 (0–1) Atmospheric and OH (6–2) airglow at lower midlatitudes, *J. Geophys. Res.*, *101*, 21,223–21,232, doi:10.1029/96JD01723.

She, C. Y., et al. (2004), Tidal perturbations and variability in mesopause region over Fort Collins, CO (41 N, 105 W): Continuous multi-day temperature and wind lidar observations, *Geophys. Res. Lett.*, *31*, L24111, doi:10.1029/2004GL021165.

Smith, S. M., S. L. Vadas, W. J. Baggaley, G. Hernandez, and J. Baumgardner (2013), Gravity wave coupling between the mesosphere and thermosphere over New Zealand, *J. Geophys. Res. Space Phys.*, *118*, 2694–2707, doi:10.1002/jgra.50263.

Swenson, G. R., and S. B. Mende (1994), OH-emission and gravity waves (including a breaking wave) in all-sky imagery from Bear Lake, UT, *Geophys. Res. Lett.*, *21*, 2239–2242, doi:10.1029/94GL02112.

Taylor, M. J., W. R. Pendleton Jr., C. S. Gardner, and R. J. States (1999), Comparison of terdiurnal tidal oscillations in mesospheric OH rotational temperature and Na lidar temperature measurements at midlatitudes for fall/spring conditions, *Earth Planets Space*, *51*, 877–885.

Torrence, C., and G. P. Compo (1998), A practical guide to wavelet analysis, *Bull. Am. Meteorol. Soc.*, *79*(1), 61–78.

Vadas, S. L., D. C. Fritts, and M. J. Alexander (2003), Mechanism for the generation of secondary waves in wave breaking regions, *J. Atmos. Sci.*, *60*, 194–214, doi:10.1175/1520-0469(2003)060<0194:MFTGOS>2.0.CO;2.

Yamada, Y., H. Fukunishi, T. Nakamura, and T. Tsuda (2001), Breakdown of small-scale quasi-stationary gravity wave and transition to turbulence observed in OH airglow, *Geophys. Res. Lett.*, *28*, 2153–2156, doi:10.1029/2000GL011945.

Yee, J. H., G. Growley, R. G. Roble, W. R. Skinner, M. D. Burrage, and P. B. Hays (1997), Global simulations and observations of O(^{1}S), O₂(^{1}Σ), and OH mesospheric nightglow emissions, *J. Geophys. Res.*, *102*, 19,949–19,968, doi:10.1029/96JA01833.

Yuan, T., et al. (2006), Seasonal variation of diurnal perturbations in mesopause region temperature, zonal, and meridional winds above Fort Collins, Colorado (40.6°N, 105°W), *J. Geophys. Res.*, *111*, D06103, doi:10.1029/2004JD005486.

Yuan, T., H. Schmidt, C. Y. She, D. A. Krueger, and S. Reising (2008), Seasonal variations of semidiurnal tidal perturbations in mesopause region temperature and zonal and meridional winds above Fort Collins, Colorado (40.6°N, 105.1°W), *J. Geophys. Res.*, *113*, D20103, doi:10.1029/2007JD009687.

Yuan, T., C. Y. She, J. Forbes, X. Zhang, D. Krueger, and S. Reising (2010), A collaborative study on temperature diurnal tide in the midlatitude mesopause region (41°N, 105°W) with Na lidar and TIMED/SABER observations, *J. Atmos. Sol. Terr. Phys.*, *72*, 541–549, doi:10.1016/j.jastp.2010.06.012.

Yuan, T., C. Fish, J. Sojka, D. Rice, M. J. Taylor, and N. J. Mitchell (2013), Coordinated investigation of summer time mid latitude descending E layer (Es) perturbations using Na lidar, ionosonde, and meteor wind radar observations over Logan, Utah (41.7°N, 111.8°W), *J. Geophys. Res. Atmos.*, *118*, 1734–1746, doi:10.1029/2012JD017845.

Zhao, Y., A. Z. Liu, and C. S. Gardner (2003), Measurements of atmospheric stability in the mesopause at Starfire optical range, NM, *J. Atmos. Sol. Terr. Phys.*, *65*, 219–232.

Zhao, Y., M. J. Taylor, and X. Chu (2005), Comparison of simultaneous Na lidar and mesospheric nightglow temperature measurements and the effects of tides on the emission layer heights, *J. Geophys. Res.*, *110*, D09S07, doi:10.1029/2004JD005115.